



HAL
open science

Thermal regime from bottom simulating reflectors along the north Ecuador-south Colombia margin; relation to margin segmentation and great subduction earthquakes

B. Marcaillou, G. Spence, J.-Y. Collot, K. Wang

► To cite this version:

B. Marcaillou, G. Spence, J.-Y. Collot, K. Wang. Thermal regime from bottom simulating reflectors along the north Ecuador-south Colombia margin; relation to margin segmentation and great subduction earthquakes. *Journal of Geophysical Research*, 2006, 111 (B12), pp.B12407. 10.1029/2005JB004239 . hal-00407607

HAL Id: hal-00407607

<https://hal.science/hal-00407607>

Submitted on 3 May 2021

HAL is a multi-disciplinary open access archive for the deposit and dissemination of scientific research documents, whether they are published or not. The documents may come from teaching and research institutions in France or abroad, or from public or private research centers.

L'archive ouverte pluridisciplinaire **HAL**, est destinée au dépôt et à la diffusion de documents scientifiques de niveau recherche, publiés ou non, émanant des établissements d'enseignement et de recherche français ou étrangers, des laboratoires publics ou privés.

Thermal regime from bottom simulating reflectors along the north Ecuador–south Colombia margin: Relation to margin segmentation and great subduction earthquakes

Boris Marcaillou,^{1,2} George Spence,³ Jean-Yves Collot,⁴ and Kelin Wang⁵

Received 21 December 2005; revised 25 May 2006; accepted 28 July 2006; published 19 December 2006.

[1] The north Ecuador–south Colombia (NESC) margin has three transverse morphotectonic segments (the Manglares, Tumaco, and Patia segments), each with different tectonic and structural patterns. Following the 1906 subduction earthquake, the NESC margin has been the site of three megathrust events in 1942, 1958, and 1979 for which the rupture zones abut one another. We first investigated variations in heat flow derived from bottom simulating reflectors (BSR) observed along multichannel seismic lines sampling the three morphotectonic segments. Strong along-strike variations of the BSR-derived heat flow, just landward of the deformation front, suggest that each morphotectonic segment has a specific thermal regime. Finite element thermal models show that these variations are mainly produced by changes in the age and the dip of the oceanic plate and local hydrothermal cooling. We then examined the relationship between seismogenesis and thermal structure along the plate boundary. The updip limits of the 1942 and 1979 seismogenic zones, estimated from the aftershock area and rupture zone, reach the trench, where the temperature at the top of the subducting plate appears to be 50°–60°C. Between these events the seismogenic zone of the 1958 earthquake is restricted to a region landward of a prominent outer basement high where the temperature appears to be 100°–120°C. We propose that on the NESC margin the updip limit of the seismogenic zone is primarily controlled by low-temperature processes except for the 1958 event for which the seismogenic updip limit appears to be related to a structural feature in the upper plate.

Citation: Marcaillou, B., G. Spence, J.-Y. Collot, and K. Wang (2006), Thermal regime from bottom simulating reflectors along the north Ecuador–south Colombia margin: Relation to margin segmentation and great subduction earthquakes, *J. Geophys. Res.*, *111*, B12407, doi:10.1029/2005JB004239.

1. Introduction

[2] In subduction zones, the updip limit of the seismogenic zone is a transition zone from shallow stable sliding (aseismic) to deeper stick slip (seismogenic) processes along the plate interface. A wide range of mechanical and chemical processes, active at temperatures of ~60° to ~150°C, have been invoked as causes of the onset of stick slip on the thrust fault. These processes include but are not limited to (1) smectite to illite transformation in the underthrust sediments at 100° to 150°C [Vrolijk, 1990], (2) shear localization and increased shear strain [Moore

and Saffer, 2001], (3) porosity reduction and increased consolidation state of gouge [Marone and Scholz, 1988], (4) increasing effective stress due to increased total overburden and possibly variations in pore pressure [Moore and Saffer, 2001] and (5) pressure solution, silica or carbonate cementation fluid release from low-temperature dehydration and hydrocarbon generation processes, and other low-temperature diagenetic alterations leading to increased gouge consolidation [Moore and Saffer, 2001; Saffer and Marone, 2003]. The downdip boundary of the seismogenic zone, which marks the transition from frictional stick slip to quasi-plastic aseismic behavior, may be explained by the onset of crystal plasticity and related creep behavior at ~350°–450°C, with the exact temperature depending upon mineralogy [Hyndman and Wang, 1993; Peacock and Hyndman, 1999; Sibson, 1982]. Nevertheless, in colder subduction zones, the intersection of the forearc mantle wedge with the subducting slab may influence the downdip limit location [Hyndman et al., 1997; Peacock and Hyndman, 1999]. Thus thermal modeling of a convergent margin aims at estimating the location of the 60°–150°C and 350°–450°C isotherms currently interpreted as related to the updip and downdip limits of the seismogenic zone. In

¹Geosciences Azur, Université Pierre et Marie Curie, Villefranche sur mer, France.

²Now at School of Earth and Ocean Science, University of Victoria, Victoria, British Columbia, Canada.

³School of Earth and Ocean Science, University of Victoria, Victoria, British Columbia, Canada.

⁴Geosciences Azur, Institut de la Recherche pour le Développement, Villefranche sur mer, France.

⁵Pacific Geoscience Center, Sydney, British Columbia, Canada.

this study we focus on the updip limit of the north Ecuador–south Colombia seismogenic zone and constrain the thermal structure with BSR-derived heat flow values.

[3] Usually great subduction earthquakes nucleate in the downdip part of the seismogenic zone with rupture propagating upward, but in some well documented cases, like Honshu (Japan) [Nagai *et al.*, 2001; Sato *et al.*, 1996], Mexico [Chael and Stewart, 1982; Valdez *et al.*, 1982] and Peru [Bourgeois *et al.*, 1999; Pelayo and Wiens, 1990; Spence *et al.*, 1999; Tavera *et al.*, 2002], great subduction events initiated at shallow depth (<30 km). These subduction zones are known to be characterized by small to medium seismic coupling ratio (α) [Pacheco *et al.*, 1993; Peterson and Seno, 1984], which is defined as the ratio of the seismic slip rate estimated from the cumulative seismic moment of large interplate earthquakes to the plate convergence rate (seismic plus aseismic slip). For $\alpha < 0.5$, hypocentral depths may show significant scatter and are not necessarily close to the bottom of the seismogenic zone [Kato and Seno, 2003].

[4] The north Ecuador–south Colombia (NESC) margin is the location of four great subduction earthquakes of the 20th century [Kanamori and McNally, 1982]. Its seismogenic zone is believed to be currently locked. Numerous multichannel seismic reflection (MCS) lines (Figure 1) acquired across this margin during the Sisteur experiment [Collot *et al.*, 2002] show a well-identified bottom simulating reflector (BSR), which represents the base of a gas hydrate layer beneath the seafloor, and extends up to 50 km landward of the trench. In the current study we use BSRs recorded on Sisteur MCS lines to assess heat flow variations. We then (1) use the heat flow values to constrain thermal modeling of the frontal part of the NESC margin, (2) locate the intersection between the seismically defined plate interface and the 60° and 150°C isotherms, (3) estimate the temperatures at which rupture initiates, and (4) discuss along-strike heat flow variations along the NESC margin in relation to its morphotectonic segmentation and the rupture zones of the 1958 and the 1979 earthquakes.

2. Geological Setting

2.1. Structure of the NESC Margin and Adjacent Nazca Plate

[5] The basement of the north Andean margin consists of mafic to ultramafic oceanic terranes [Goosens and Rose, 1973; Juteau *et al.*, 1977] intruded by intraoceanic volcanic rocks [Cosma *et al.*, 1998; Evans and Whittaker, 1982] and accreted to the paleo–South American margin during the Cretaceous to Paleogene times [Gansser, 1973; Toussaint and Restrepo, 1994]. The oceanic basement is overlain by a Cretaceous volcanosedimentary sequence and a thick Cenozoic forearc sedimentary basin [Deniaud, 2000; Jaillard *et al.*, 1995].

[6] The NESC margin displays wide along-strike variations in structural character. The Patia Promontory to the north and the Esmeraldas Promontory to the south bracket an up to 80 km wide, 800–1000 m deep morphologic reentrant, named the Tumaco reentrant (Figure 1). Seismic reflection lines SIS-24 and SIS-32, crossing the interpreted boundary between the 1958 and 1979 earthquake rupture

zones (Figure 2), provide evidence for a N106° trending major crustal fault, the Manglares Fault, cutting transversely across the forearc basin [Collot *et al.*, 2004]. As described in detail in this previous study, the Manglares Fault divides two margin segments with drastically different tectonic regimes. South of the fault the subsiding forearc basin is wide and largely nondeforming (line SIS-45 of Collot *et al.* [2004]) whereas north of the fault the margin is severely folded, shortened and uplifted (line SIS-35 of Collot *et al.* [2004]). These authors also described the strong influence of a prominent outer basement high (OBH) that fronts the Manglares margin segment at the seaward limit of the rupture propagation of the 1958 event (Figure 2). Lines SIS-47 and SIS-42 (Figures 3b and 3c) are located in the Tumaco and Manglares segments, respectively. The Patia promontory defines a drastic morphological and bathymetric change along the margin (Figure 1). Furthermore, in seismic lines SIS-39 and SIS-40 (Figure 3a) off the Patia Promontory, the margin is fronted by a 35 km wide accretionary prism whereas lines off the Tumaco reentrant present a less than 5 km wide accretionary prism (Figure 3b) or no prism (Figure 3c). Thus marine geophysical data collected during the Sisteur cruise highlight a tectonic and structural segmentation of the NESC margin into four morphotectonic segments (Figure 1). To the south, the Esmeraldas Promontory is associated with the northern boundary of the Esmeraldas segment, which is not examined in this paper. Northward, the Manglares fault divides the Tumaco reentrant into the Manglares and Tumaco segments. Moreover, the OBH fronting the Manglares margin segment appears to influence strongly the coseismic rupture propagation of the 1958 earthquake [Collot *et al.*, 2004]. To the north, the Patia Promontory defines the Patia segment that tectonically differs from the other segments by the well-established accretionary regime.

[7] The Nazca Plate underthrusts the north Andean margin at a rate of 5.4 cm yr⁻¹ in an eastward direction [Trenkamp *et al.*, 2002]. Magnetic lineations 5A to 6A trend WNW east of the Yaquina Graben and extend beneath the NESC margin (Figure 4), subperpendicular to the trench. They indicate a southward aging of the Nazca Plate from ~12 to 20 Ma [Hardy, 1991] in the study area. Moreover, all the MCS lines sampling the Tumaco central segment show numerous normal faults in the crust of the Nazca Plate beneath the trench and just landward of it (Figure 3b). In contrast, in the Manglares and Patia segments, the Nazca Plate is not or only slightly faulted (Figures 3a and 3c).

2.2. NESC Subduction Earthquakes

[8] On the Andean margin, north of the Carnegie Ridge, plate convergence produced four great subduction earthquakes during the 20th century [Kanamori, 1986; Kanamori and Given, 1981; Thatcher, 1990] (Figure 2). This sequence of large ruptures shows characteristics that may be explained by variations in crustal structure and thermal regime. The largest event (Mw = 8.8) occurred in 1906 [Kanamori and Given, 1981; Kanamori and McNally, 1982] and ruptured a segment of the margin about 500 km in length [Kelleher, 1972]. Three smaller thrust events reactivated adjacent segments within the 1906 rupture zone [Mendoza and Dewey, 1984]. From south to north, they

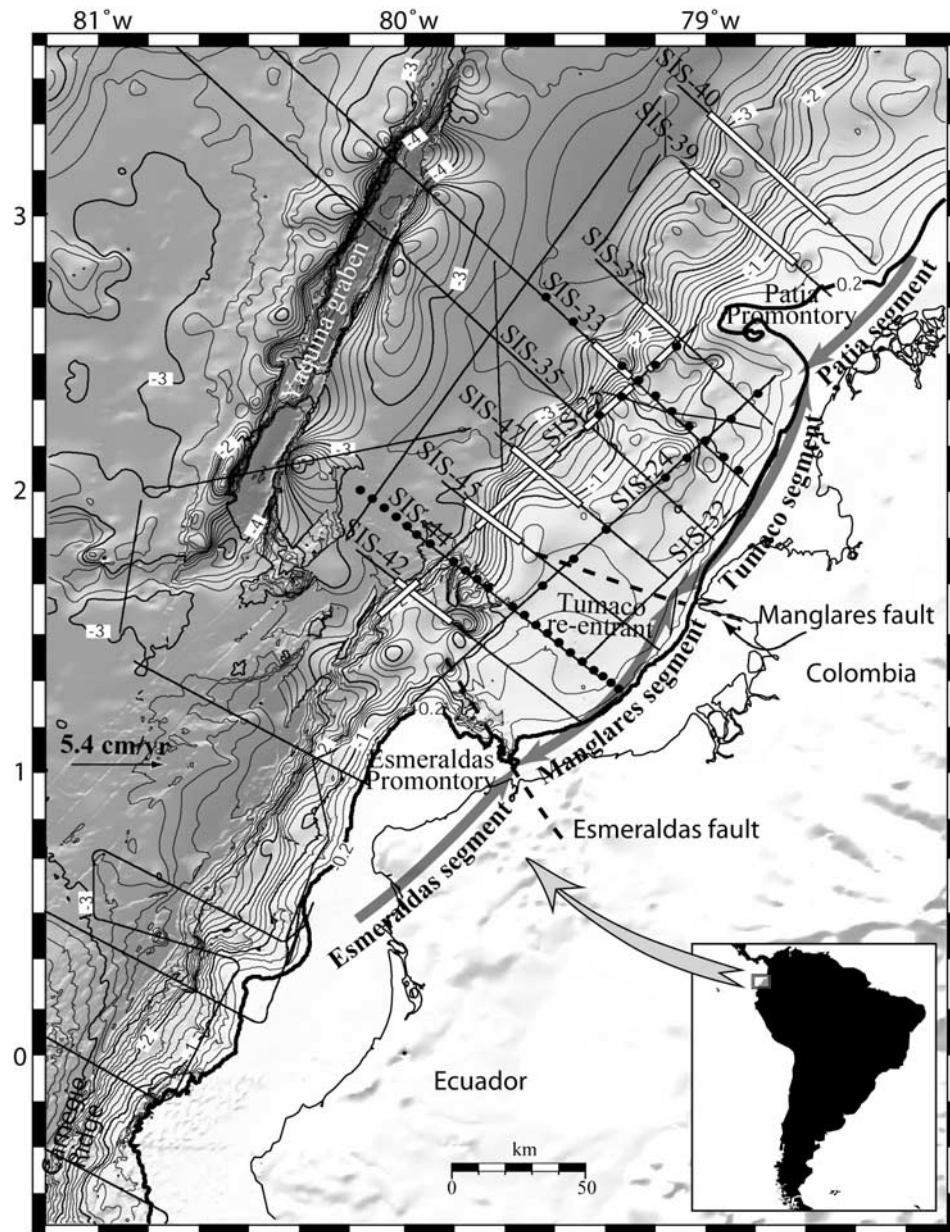


Figure 1. Bathymetric map of the north Ecuador–south Colombia margin and the adjacent Nazca Plate, after *Collot et al.* [2004]. Contours are in km, and the 0.2 km bold isobath highlights the Tumaco Reentrant bounded by the Patia and Esmeraldas Promontories. The thin black lines are Sisteur MCS profiles, and the thick white lines are MCS sections with BSRs identified with confidence. Solid circles represent the locations of ocean bottom seismometers on four wide-angle lines recorded during the Sisteur and Salieri experiments. The single arrow is Nazca–South America plate convergence vector derived from GPS studies [*Trenkamp et al.*, 2002]. Double arrows indicate the morphotectonic segmentation of the margin.

occurred in 1942 ($M_w = 7.9$) [*Swenson and Beck*, 1996], 1958, ($M_w = 7.8$) and 1979 ($M_w = 8.2$) [*Beck and Ruff*, 1984; *Herd et al.*, 1981; *Kanamori and McNally*, 1982]. Each main shock is located in a central portion of the aftershock area [*Mendoza and Dewey*, 1984]. The seismic coupling ratio based on the great 1979 Colombia earthquake alone with an assumed recurrence interval of 70 years was estimated to be 0.33 [*Beck and Ruff*, 1984], which is consistent with a possible location of the hypocenter in a

central to shallow area of the seismogenic zone [*Kato and Seno*, 2003]. The southern limits of the 1942 and 1906 rupture zones are located near the northern flank of the Carnegie ridge that appears to act as a barrier. The 1942 rupture and the 1958 rupture [*Mendoza and Dewey*, 1984] meet at the Esmeraldas fault dividing the Esmeraldas and Manglares segments (Figure 2). In contrast, the northern limit of the 1958 rupture is located about 60 km south of the 1979 asperity [*Beck and Ruff*, 1984]. On the basis of Sisteur

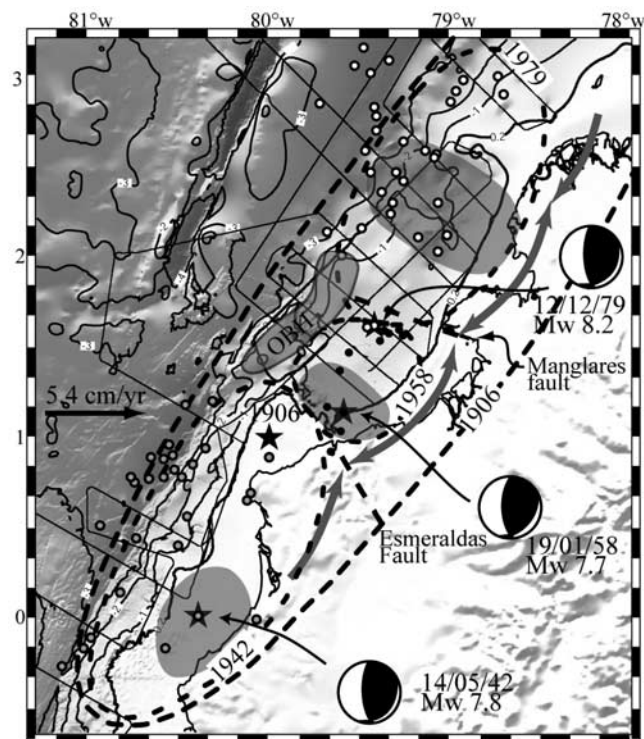


Figure 2. Location of the epicenters (stars), rupture zones (dashed ellipses), asperities (gray ellipses), and focal mechanisms of the 20th century great subduction earthquakes that occurred beneath the NESM margin [Collot *et al.*, 2004]. Gray, solid, and open circles are the 1942, 1958 and 1979 aftershocks, respectively. OBH is the outer basement high, defining the seaward boundary of the 1958 rupture zone [Collot *et al.*, 2004]. Double arrows indicate the morphotectonic segmentation of the margin (Figure 1).

MCS data, Collot *et al.* [2004] proposed that the Manglares fault may correlate with the boundary between the 1958 and 1979 rupture zones, and acts as a barrier to coseismic strain release. Using a model incorporating spatial variation in moment release, Beck and Ruff [1984] showed that the 1979 subduction earthquake ruptured the Tumaco and Patia tectonic segments as far seaward as the deformation front. In contrast, the seaward limit of the 1958 rupture zone, located along the landward side of a major outer basement high (OBH) about 25 km landward of the trench, may have been controlled by a megathrust splay fault [Collot *et al.*, 2004]. The propagation of the coseismic rupture possibly close to the deformation front along the thrust fault, as in 1906 and 1979 [Beck and Ruff, 1984], or up to the seafloor along a splay fault as in 1958 [Collot *et al.*, 2004], may have triggered tsunamis [Abe, 1979; Kanamori and McNally, 1982; Lockridge and Smith, 1984]. Modeling thermal regime spatial variations may help understand factors controlling the coseismic slip propagation.

3. BSR-Derived Heat Flow

3.1. Method

[9] The BSR (Figure 3) has been widely interpreted as the base of the stability field for methane hydrate [Shipley *et al.*,

1979]. Heat flow values at the seafloor can be inferred from the vertical traveltimes of the seafloor and the BSR reflectors [Townend, 1997; Yamano *et al.*, 1982] as the product of thermal conductivity and thermal gradient between the BSR and the seabed. Thermal conductivity is estimated to vary from $0.9 \text{ W m}^{-1} \text{ } ^\circ\text{C}^{-1}$ near the sea bottom to $1.15 \text{ W m}^{-1} \text{ } ^\circ\text{C}^{-1}$ at 500 m depth, based on an empirical expression calculated from Leg 112 data on the Peruvian margin [Suess and von Huene, 1988]. Temperature at the trench seafloor was measured using a CTD profiler [Flueh *et al.*, 2001], and this temperature-depth profile was used to specify seafloor temperatures for shallower water depths. The conversion of traveltimes to BSR depth below the seafloor was determined by using a general velocity function for upper terrigenous sediments [Hamilton, 1980] which was confirmed by velocity analysis conducted on MCS data. The pressure at the BSR depths is calculated assuming a hydrostatic pressure within the sediment column. The corresponding temperatures at the BSR are obtained using the methane hydrate temperature-pressure phase diagram in a pure methane-seawater system [Dickens and Quinby-Hunt, 1994].

3.2. Uncertainties in the BSR-Derived Heat Flow

3.2.1. Fluid Flow

[10] We have assumed conductive heat flow in the BSR areas. If significant advective heat flow is present, the theoretical stability curve may not be applicable [Ruppel, 1997; Xu and Ruppel, 1999] and the heat flow at the seafloor may be significantly different. However, even near the deformation front where fluid flux is largest, the maximum variations in heat flow due to compaction-driven diffuse fluid flow is less than 5% [Wang *et al.*, 1993].

3.2.2. Picking Error

[11] Uncertainty in picking the traveltimes of the BSR and seafloor reflections may lead to an error less than 8 ms on each reflector, and to a total error of about 5–8% for the BSR depths below seafloor.

3.2.3. Sediment Velocity

[12] The calculated heat flow is not very sensitive to sediment velocity variations [Ganguly *et al.*, 2000]. An increase in the depth of the BSR will also produce an increase in temperature at the BSR, and thus will have little influence on the temperature gradient [Henry *et al.*, 2003].

3.2.4. Lithostatic Versus Hydrostatic Pressures

[13] Another source of error may come from the choice of hydrostatic pressure in the sediment pore space, which may lead to underestimation if the pressure is higher or even lithostatic. This underestimation ranges from ~2% for the large water depths found in the trench, which is the area of interest in this paper, to a maximum value of 10% in shallow water [Ganguly *et al.*, 2000].

3.2.5. Thermal Conductivity

[14] Since the conductivity is inferred from measurements available on the Peruvian margin, it is difficult to evaluate the error it causes; we assign an error of 10%, consistent with estimates by Ganguly *et al.* [2000].

[15] Thus the total error (root-mean-square of all errors) in our heat flow may reach 20%, similar to those of other BSR studies [Ganguly *et al.*, 2000; Henry *et al.*, 2003; Townend, 1997]. However, the relative error in heat flow, which applies when making comparisons between nearby

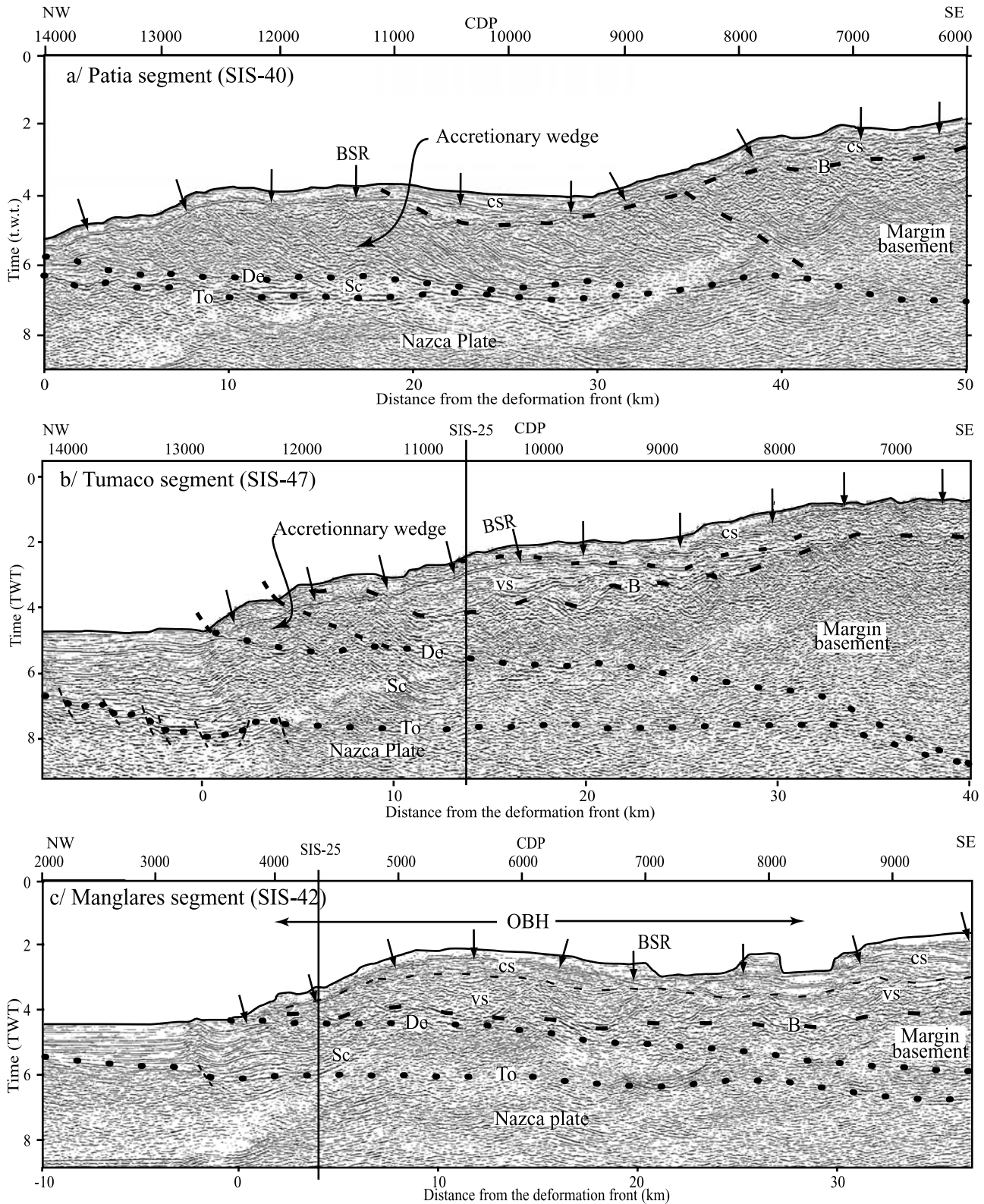


Figure 3. MCS lines SIS-40, SIS-47, and SIS-42 showing structures of the (a) Patia, (b) Tumaco, and (c) Manglares margin segments, respectively. Arrows point to the BSR. De is the interplate décollement, To is top of underlying oceanic crust, and B is top of margin basement. Sc is the subduction channel. Margin sediments include Cenozoic forearc units (cs) and a Cretaceous volcanosedimentary unit (vs).

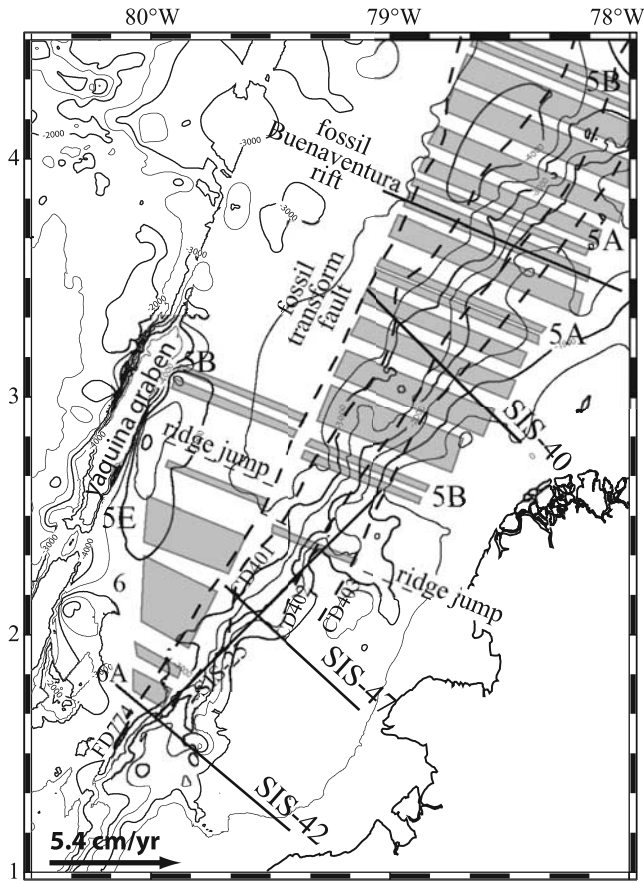


Figure 4. Nazca Plate magnetic lineations identified between the Yaquina Graben and NESC margin [Hardy, 1991]. Dashed lines are magnetic anomaly ship tracks, and solid lines are Sisteur MCS lines used in this paper.

regions, is perhaps 10% or less, much smaller than the absolute error.

3.3. Heat Flow Variations

[16] Heat flow profiles were calculated as a function of the distance to the deformation front along the seven seismic dip lines for which a BSR could be confidently identified (Figure 5). At the deformation front of the Patia, Tumaco and Manglares segments, the BSR depth ranges from ~80 to ~110 ms, ~210 to ~250 ms, and ~230 to 280 ms below the seafloor, respectively. It is significant that, within the first 25 km of the deformation front, the heat

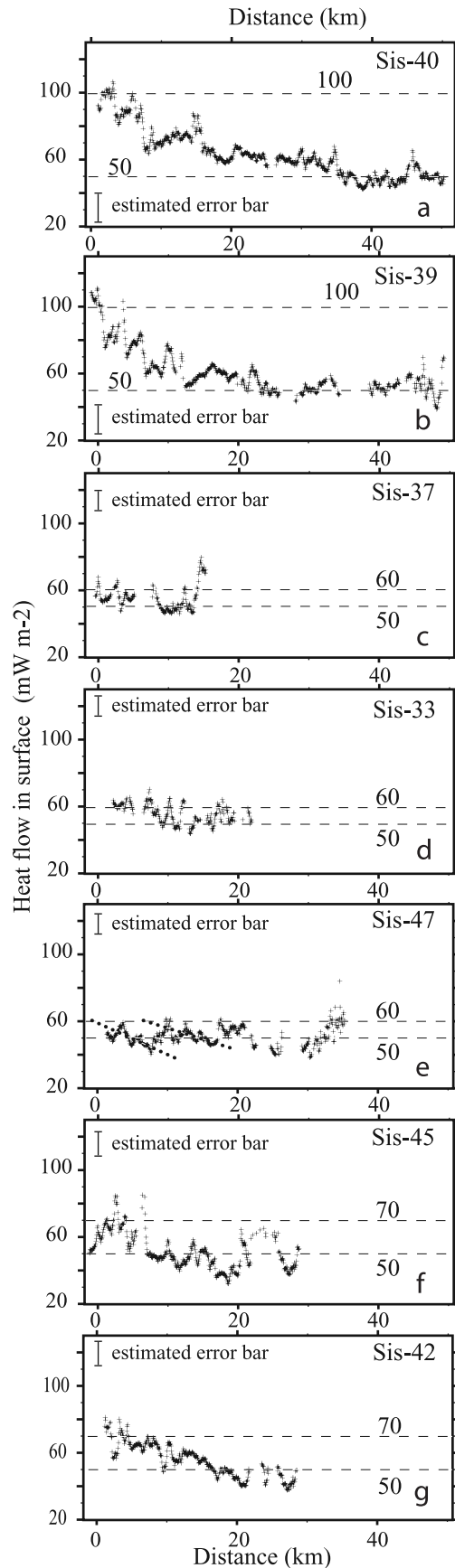


Figure 5. BSR-derived heat flow versus distance from the deformation front along selected Sisteur MCS lines. Location is shown in Figure 1. Note that lateral heat flow gradients and average maximum values at the margin front are similar within three groups of lines: (1) SIS-39 and SIS-40, (2) SIS-37, SIS-33, and SIS-47, and (3) SIS-45 and SIS-42, which are associated with the Patia, Tumaco, and Manglares morphotectonic segments of the margin thermal modeling, respectively. Note also that for line SIS-47 the BSR-derived heat flow between km 0 and km 10 is ~15 mW m⁻² lower than between km 10 and km 20 (highlighted by dashed lines).

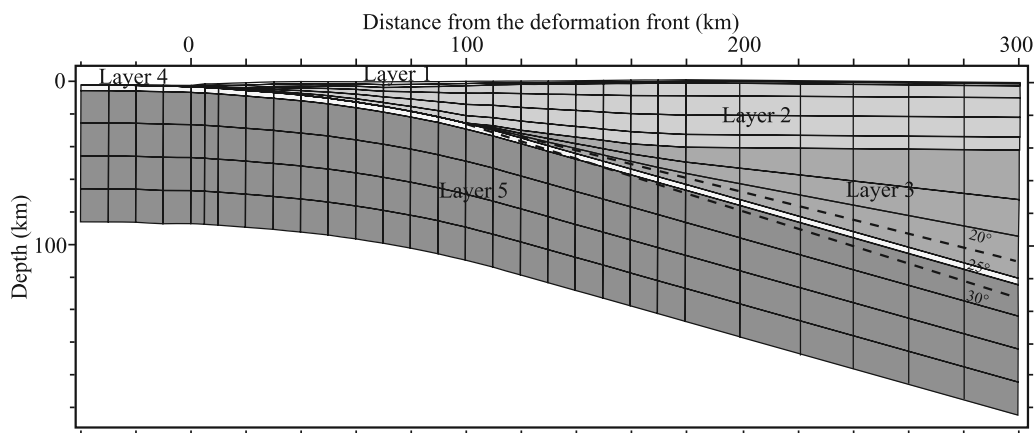


Figure 6. Finite element mesh used for thermal modeling along profile SIS-47. Layers 1–5 represent (1) the sediments (accretionary wedge, forearc basin, and underlying volcanosedimentary sequence), (2) the margin oceanic basement, (3) the upper plate mantle, (4) the subducting sediments, and (5) the downgoing lithosphere, which dips landward at $\sim 25^\circ$. Two other dip values (20° and 30° shown by dashed lines) have been tested in order to estimate uncertainties in this parameter (Figure 7).

flow varies from one margin segment to the other. Across the Patia segment, profiles SIS-39 and 40 (Figure 5) show remarkably coherent heat flow values that decrease rapidly from $100\text{--}110\text{ mW m}^{-2}$ at the deformation front to $50\text{--}60\text{ mW m}^{-2}$ at locations 20 km farther landward (Figures 5a and 5b). In the Tumaco segment (Figure 1), heat flow values along lines SIS-37, 33 and 47 (Figures 5c, 5d, and 5e) are consistent and decrease slowly from about 60 mW m^{-2} near the deformation front to $50\text{--}55\text{ mW m}^{-2}$ landward (Figure 5c). Across the Manglares segment, lines SIS-45 and SIS-42 show coherent heat flow values reaching $70\text{--}80\text{ mW m}^{-2}$ near the deformation front (Figures 5f and 5g). The differences between the heat flow values at the deformation front of each segment are much larger than the estimated errors of the BSR-derived heat flow. The variations in the thermal regime along the margin suggest that each morphotectonic segment of the margin has a characteristic thermal structure. As MCS lines with the longest reliable BSRs, profiles SIS-40, SIS-47, and SIS-42 (Figure 3) were chosen to represent respectively the whole Patia, Tumaco and Manglares segments.

4. Thermal Modeling

[17] We used a two-dimensional steady state finite element model [Wang *et al.*, 1995a] to predict the heat flow at the seafloor and to compare the theoretical values with observed values derived from the BSRs. Heat transfer above the subducting plate is assumed to be purely conductive, but plate subduction causes downward advection of heat. This approach has been applied to a number of margins such as Cascadia [Hyndman and Wang, 1993; Wang *et al.*, 1995b], Japan [Hyndman *et al.*, 1995], Chile, Alaska [Oleskevich *et al.*, 1999], Mexico [Currie *et al.*, 2002], and Costa Rica [Harris and Wang, 2002].

4.1. Model Geometry and Convergence Rate

[18] The finite element mesh, which extends from 40 km seaward of the deformation front to 300 km landward, is composed of five layers (Figure 6). Layer 1 represents a

highly compacted sedimentary sequence including the accretionary wedge, the Cenozoic forearc basin and underlying Cretaceous volcanosedimentary sequence. Layer 1 thicknesses typically range from 2 km to 5 km, and by 1 km depth all sediments are sufficiently compacted to have thermal conductivities above $2\text{ W m}^{-1}\text{ K}^{-1}$ (see section 4.3 on thermal parameters). We think it is reasonable to combine the thin slope sediments and other unconsolidated near-surface sediments into this layer. Layer 2 represents the upper plate basement, known to be an oceanic complex in the study area. Layer 3 represents the continental mantle wedge. Layer 4 represents subducted sediments. Layer 5 is the oceanic lithosphere. Oceanic crust and lithospheric mantle are assigned the same thermal parameters, so the boundary between them is not present in the thermal model.

[19] The structure of the Ecuador–Columbia margin is very well defined with bathymetric data and results of seismic surveys with recordings on the seafloor and land. In order to define the geometry and the thickness of each layer we used (1) MCS data for the shallow and intermediate structure of the margin wedge, (2) wide-angle seismic results [Agudelo, 2005; Agudelo *et al.*, 2002; Gailler *et al.*, 2003, 2004; Meissner *et al.*, 1976] and prestack depth migration of selected lines [Agudelo *et al.*, 2005; Marcaillou *et al.*, 2005] for a time to depth conversion of MCS lines, the deep crustal structure, the slab dip at shallow to intermediate depth and the forearc Moho location, and (3) intermediate-depth earthquake locations to estimate the dip angle of the downgoing slab down to 50 km. This dip is $\sim 25^\circ$ [Engdahl *et al.*, 1998] (Figure 7). To estimate uncertainties in predicted heat flow for each margin segment, the dip of the slab was varied between 20° and 30° (Figure 6). Our results indicated that, although the thermal structure of the landward part of the model strongly depends on the dip of the slab, this parameter has a negligible influence on heat flow values calculated within 50 km of the deformation front, where the greatest variations in BSR-derived heat flow occur.

[20] Calculated heat flow is very sensitive to the geometry and rock physical properties near the deformation front,

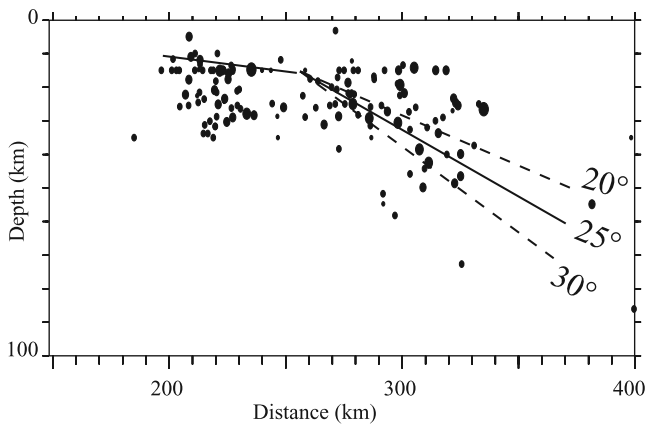


Figure 7. Earthquake hypocenters along a 100 km wide corridor centered along line SIS-33 [Engdahl *et al.*, 1998]. The Wadati-Benioff zone dips $\sim 25^\circ \pm 5^\circ$.

as described in detail by Marcaillou [2003]. For each segment, we constructed a mesh (Figure 8) based on the structural interpretation of MCS lines SIS-40, SIS-47, and SIS-42 (Figure 3). During the Sisteur and Salieri experiments, four wide-angle lines, two parallel and two perpendicular to the NESZ margin, were recorded (Figure 1). Structural models derived from these seismic data provide accurate velocity versus depth relations along these lines [Agudelo, 2005; Agudelo *et al.*, 2002; Gailler *et al.*, 2003, 2004]. We used the refraction velocity structures to calculate a time to depth conversion of MCS lines SIS-40, SIS-47, and SIS-42 in order to construct the related grids.

[21] Within 40 km landward of the deformation front, the seafloor morphology varies significantly among different cross sections. On line SIS-47, the outer continental slope is relatively smooth (Figure 3b), while on line SIS-40 a prominent slope break occurs at 30 km from the deformation front (Figure 3a). On line SIS-42, the slope dips steeply trenchward within the first 10 km of the deformation front but becomes flat or dips slightly landward farther east (Figure 3c). This topography delineates the outer basement high that is a characteristic of the Manglares segment (Figures 2 and 3) [Collot *et al.*, 2004]. A second critical difference between the cross sections is the average dip of the décollement beneath the frontal part of the margin. The dip is $\sim 6.5^\circ$, $\sim 11^\circ$ and $\sim 7.5^\circ$ within 50 km of the deformation front for lines SIS-40, SIS-47, and SIS-42, respectively. The dip depends on (1) the depth to the top of crust of the incoming Nazca Plate (layer 5) and (2) the thickness variations of the subducted sediments (the “subduction channel”) (layer 4). On line SIS-47, the depth of 7.6 km to the top of layer 5 beneath the deformation front is 2 km and 2.1 km deeper than on lines SIS-40 and SIS-42, respectively. Moreover, layer 4 for line SIS-47 is very thick because the ~ 4.4 km thick trench fill is entirely subducted. The trench fill is only ~ 1.8 km for line SIS-40 and ~ 2.7 km for line SIS-42. On SIS-40, very little sediment is subducted, so layer 4 is very thin. The third major difference between the three cross sections is the distance from the deformation front to the first occurrence of layer 2 or upper plate basement. In the Patia segment, line SIS-40 indicates a 35 km wide accretionary wedge found landward of the

deformation front [Marcaillou, 2003; Mountney and Westbrook, 1997]. In contrast, in the Tumaco segment, line SIS-47 shows that layer 2 extends trenchward to less than 10 km from the deformation front, where the basement is fronted by a small accretionary wedge [Marcaillou, 2003]. In the Manglares segment, line SIS-42 shows no clear evidence for an accretionary wedge; rather, the Cenozoic forearc basin and underlying Cretaceous volcanosedimentary sequence, all parts of a thick layer 1, extend seaward to near the deformation front [Marcaillou, 2003]. Layer 2, which represents the upper plate basement, also extends to 10 km from the deformation front.

[22] Elements in layers 4 and 5 are assigned a uniform downdip velocity corresponding to the convergence rate, while elements in the other three layers are fixed. Beneath the north Andean margin, the Nazca oceanic plate subducts at a rate of 5.4 cm yr^{-1} in a $N90^\circ$ direction relative to the fixed Brazilian shield [Trenkamp *et al.*, 2002]. The margin-normal component of the convergence velocity of 5.0 cm yr^{-1} is used for the model.

4.2. Boundary Conditions

[23] The lateral heat flow across the vertical landward boundary, far from the region of interest around the updip end of the seismogenic zone of the megathrust, is taken to be zero. Our results indicate that the condition assigned to this boundary has a negligible influence on heat flow values calculated within 50 km of the deformation front, where the greatest variations in BSR-derived heat flow occur. The upper boundary of the model is set at 2°C which is

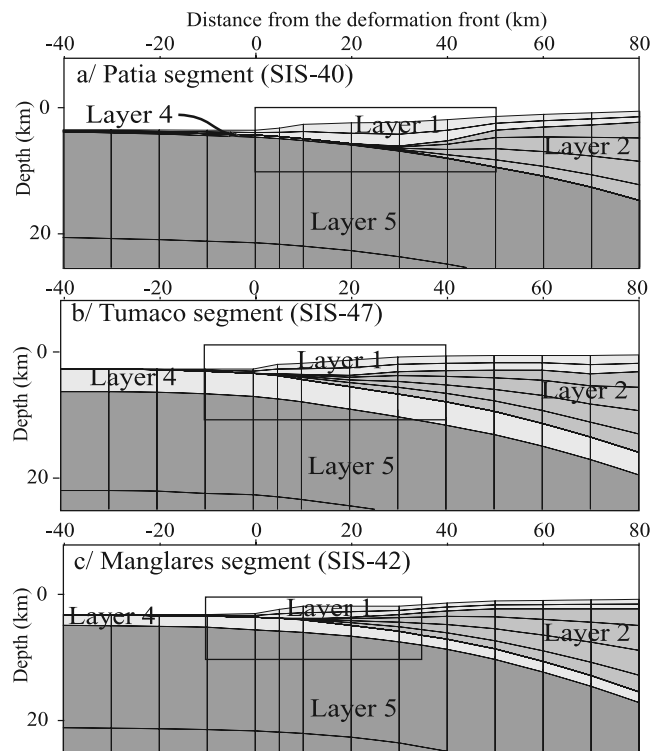


Figure 8. Details of finite element meshes for models along MCS lines (a) SIS-40, (b) SIS-47, and (c) SIS-42. Rectangles indicate locations of the seismic sections shown in Figure 3.

Table 1. Thermal Parameters Used in the Thermal Modeling of the NESC Margin^a

Layer	Rock Type	Thermal Conductivity λ , $\text{W m}^{-1} \text{K}^{-1}$	Heat Generation Q , $\mu\text{W m}^{-3}$	Thermal Capacity, $\text{MJ m}^{-3} \text{K}^{-1}$
1	compacted sediments	1.5, 2.0, and 2.5	0.5, 1.0, and 1.5	3.3
2	continental crust	2.0, 2.5, and 3.0	0.01, 0.05, and 0.1	3.3
3	continental mantle	3.3	0.01	3.3
4	subducting sediments	3.5	0.5, 1.0, and 1.5	3.3
5	oceanic lithosphere	2.9	0.02	3.3

^aIn our models the thermal conductivity and heat generation of the layers 1, 2, and 4 were tested for three different values.

the seafloor temperature for depths greater than ~ 2000 m as determined by CTD records [Flueh *et al.*, 2001]. Seafloor temperature is slightly higher on the upper slope or shelf region and on land, but neglecting this small variation will have little effect on heat flow near the deformation front, which is the focus of the study. The base of the model, set at 100 km depth, is fixed at 1450°C , which approximates the mantle temperature at the base of the lithosphere. The basal temperature condition has little influence on model results because the main control on the thermal regime is provided by the seaward boundary conditions, i.e., the thermal structure of the incoming oceanic plate that depends mainly on the age of the plate [K. Wang *et al.*, 1995].

[24] The temperature-depth profile of the incoming plate is obtained using a one-dimensional finite element model of a cooling lithosphere [Wang and Davis, 1992]. The sedimentation rate is neglected. We think that the age variations of ~ 12 to 20 Ma (Figure 4) [Hardy, 1991] at the trench is a reasonable assumption because magnetic lineations trend subperpendicular to the trench, and the convergence is roughly eastward. Moreover, the interpreted WNW trending fossil Buenaventura Rift intersects the trench to the north of our study area (3.5° to 4°N). As a consequence, the subducting oceanic crust is ~ 12 Myr old (anomaly 5A) on line SIS-40, ~ 16 Myr (anomaly 5E) on line SIS-47, and ~ 19 Myr (anomaly 6A) on line SIS-42 (Figure 4). However, the MCS lines are not fully parallel to the magnetic lineations, and magnetic lineations are not strictly collinear with the plate convergence vector, such that the Nazca plate age increases slightly along each seismic profile, and the plate age varies by ~ 2 Myr within each margin segment. We thus allowed variations of ± 2 Myr in order to estimate uncertainties associated with the plate age.

4.3. Thermal Parameters

[25] Each element is assigned a uniform thermal conductivity, heat generation and thermal capacity. On the NESC margins, no measurements of these parameters currently exist, so estimates were taken from the literature. Although thermal conductivity for unconsolidated sediments is near $1.0 \text{ W m}^{-1} \text{K}^{-1}$ near the seafloor, it increases rapidly with depth as porosity decreases, and may reach a value of 2.0 – $3.0 \text{ W m}^{-1} \text{K}^{-1}$ at depth [Beardsmore and Cull, 2001; Clauser and Huenges, 1995; Turcotte *et al.*, 1978]. Previous thermal models assume average values ranging from 1.5 to $2.5 \text{ W m}^{-1} \text{K}^{-1}$. In layer 1, to estimate the range of error associated with sediment conductivities, we test values of 1.5 , 2.0 , and $2.5 \text{ W m}^{-1} \text{K}^{-1}$ (Table 1). Because subducting sediments in layer 4 are progressively compacted and dewatered beneath the deformation front, we use thermal conductivity values as high as $2.5 \text{ W m}^{-1} \text{K}^{-1}$, as found in

the literature [Beardsmore and Cull, 2001]. Layer 2 represents the upper plate basement known to be an oceanic complex composed of mafic to ultramafic rocks, with thermal conductivities of about 2.0 to $2.5 \text{ W m}^{-1} \text{K}^{-1}$ [Clauser and Huenges, 1995] or $\sim 2.0 \text{ W m}^{-1} \text{K}^{-1}$ [Beardsmore and Cull, 2001]. Previous thermal models assume for the oceanic crust average thermal conductivities ranging from 2.0 to $3.0 \text{ W m}^{-1} \text{K}^{-1}$ [Dumitru, 1991; Hyndman and Wang, 1993; Oleskevich *et al.*, 1999]. To assess the influence of thermal conductivity value in layer 2 on model results, we test three values: 2.0 , 2.5 and $3.0 \text{ W m}^{-1} \text{K}^{-1}$ (Table 1). For the continental mantle (layer 3) and the incoming lithosphere (layer 5), we use thermal conductivities 3.1 and $2.9 \text{ W m}^{-1} \text{K}^{-1}$, respectively, as commonly used in previous thermal modeling studies [Heasler and Surdam, 1985; Van den Beukel and Wortel, 1988].

[26] The radiogenic heat production in the sediments and basement rocks is poorly known. For sediment layer 1 and layer 4 we test values of 0.5 , 1.0 and $1.5 \mu\text{W m}^{-3}$ (Table 1) which are consistent with the range of values selected for most previous thermal studies [Dumitru, 1991; Hyndman and Wang, 1993; Oleskevich *et al.*, 1999]. Mafic to ultramafic rocks are known for their low composition in radioactive isotopes and thus for their low heat generation: around $0.11 \pm 0.13 \mu\text{W m}^{-3}$ for gabbros and $0.01 \pm 0.01 \mu\text{W m}^{-3}$ for basalts [Brown and Mussett, 1993; Cermak *et al.*, 1990]. In our study, we use values of 0.01 , 0.05 and $0.1 \mu\text{W m}^{-3}$ to test the influence of the heat generation of the layer 2 on the thermal regime (Table 1). For heat generation in the continental mantle (layer 3) and the subducting plate (layer 5), we chose values of 0.01 and $0.02 \mu\text{W m}^{-3}$, respectively, based on values commonly used in most previous thermal studies.

[27] We use the most common value of thermal capacity assumed in previous studies, $3.3 \text{ MJ m}^{-3} \text{K}^{-1}$ (Table 1). It has been shown that reasonable modifications in its value generate negligible variations in the thermal modeling results [Hyndman and Wang, 1995].

5. Results and Discussions

5.1. Calculated Heat Flow and Temperature

[28] Calculated heat flow versus distance from the deformation front for each model profile is shown in Figure 9. The effects of variations in plate dip (Figure 7), slab age (Figure 4) and thermal parameters (Table 1) on the calculated heat flow were tested by Marcaillou [2003] and are further examined in this work. These tests provide an overall error estimate for the calculated heat flow reaching a maximum value of $\pm 6 \text{ mW m}^{-2}$ between km 15 and km 25 on the SIS-40 heat flow profile (Figure 9a). Along the

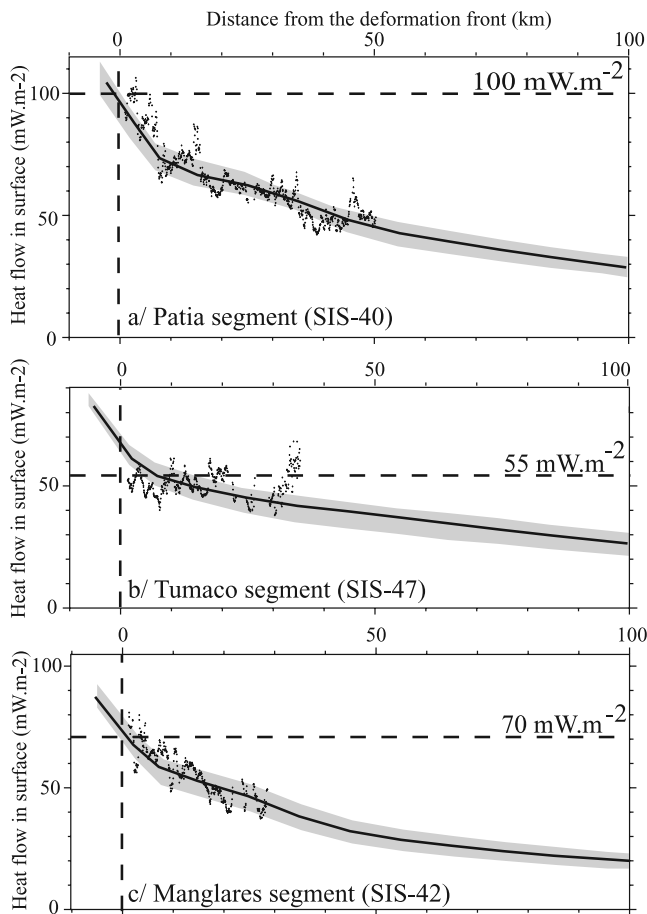


Figure 9. BSR-derived heat flow (dots) and calculated heat flow (solid line) along lines (a) SIS-40, (b) SIS-47, and (c) SIS-42. Shaded areas indicate the estimated error on the calculated heat flow based on sensitivity tests using different thermal parameter values (see section 4.3).

three modeled profiles, the calculated heat flow at the deformation front is $\sim 100 \text{ mW m}^{-2}$ for SIS-40, and $\sim 70 \text{ mW m}^{-2}$ for SIS-47 and SIS-42 lines. Beyond a distance of 25 km landward of the deformation front, calculated heat flow values are 40 to 50 mW m^{-2} and are similar for all three profiles (Figure 9). Thus the models show a reasonable agreement between the long-wavelength BSR-derived heat flow and the calculated heat flow. However, on line SIS-47, the calculated heat flow within 10 km of the deformation front is $\sim 15 \text{ mW m}^{-2}$ higher than the BSR-derived heat flow (Figure 9b), which, in turn, is abnormally low compared to the area between km 10 and km 20 (highlighted using dotted lines in Figure 5). This suggests possible local perturbations as discussed later in the text.

[29] Temperature contours of 50° to 1200°C are shown in Figure 10 for all three model sections. Table 2 and Figures 10 and 11 give the location of the 60° and 150°C temperatures along the plate interface with error estimates. These temperatures are located at similar depths and distances from the trench in the Patia (SIS-40) and Tumaco (SIS-47) segments, whereas they are located more landward in the Manglares segments (SIS-42).

5.2. Possible Origins of Along-Strike Heat Flow Variations

5.2.1. Influence of the Age of the Nazca Plate

[30] In our modeling, we have assigned to the subducting slab an age of $12 \pm 2 \text{ Ma}$ for line SIS-40, $16 \pm 2 \text{ Ma}$ for line SIS-47 and $19 \pm 2 \text{ Ma}$ for line SIS-42 (Figure 4) [Hardy, 1991]. On the basis of a theoretical relation between plate age and oceanic heat flow [Stein and Stein, 1992], the heat flow should decrease from $\sim 130 \text{ mW m}^{-2}$ for a 12 Myr old oceanic plate to 110 mW m^{-2} for a 16 Myr old plate and 100 mW m^{-2} for a 19 Myr old plate. This heat flow–age relation is already built into the boundary conditions we applied to the seaward boundary of the model. Thus along-strike age variations can account for only $\sim 20 \text{ mW m}^{-2}$ of the observed heat flow decrease from 100–110 mW m^{-2} to 50–60 mW m^{-2} between the Patia and Tumaco segments. Most of the decrease must have other reasons. Similarly, the heat flow increase from 50–60 to 70–80 mW m^{-2} from the Tumaco to the Manglares segments is opposite to the decreasing trend of plate age, again suggesting additional causes for local heat flow variations. Thus the southward increase of the Nazca Plate age fails to explain all the

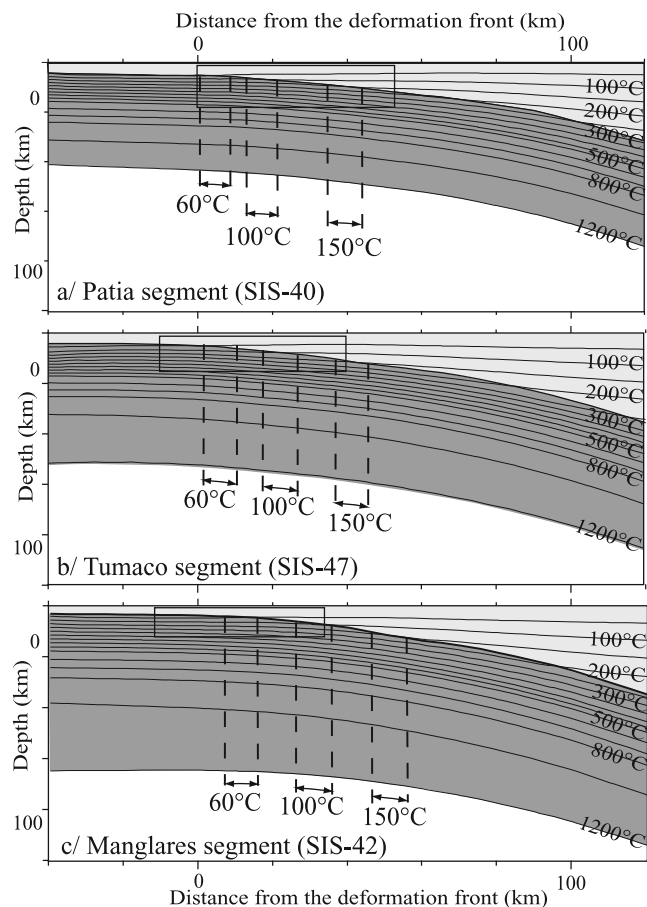


Figure 10. Thermal structure of the frontal part of the margin for (a) Patia segment (line SIS-40), (b) Tumaco segment (line SIS-47), and (c) Manglares segment (line SIS-42) and the location of the 60°, 100°, 150°C isotherms on the thrust faults and associated uncertainties. Rectangles indicate locations of the seismic sections shown in Figure 3. The actual finite element mesh extends to 180 km depth.

Table 2. Depths and Distances From the NESC Deformation Front of the Intersection Point Between the Plate Interface and Isotherms 60° and 150°C

	SIS-40		SIS-47		SIS-42	
	Depth, km	Distance, km	Depth, km	Distance, km	Depth, km	Distance, km
60°C	5 ± 0.5	4 ± 3	5 ± 0.5	5 ± 3	5 ± 0.5	9 ± 3
150°C	9.5 ± 1	38 ± 4	11 ± 1	40 ± 4	14 ± 1	51 ± 4

variations of the heat flow values at the deformation front of the NESC margin.

5.2.2. Influence of the Dip of the Nazca Plate

[31] Figure 12 graphically illustrates the along-strike variations of basement depth, slab dip and trench fill thickness and their influence on the heat flow values. Beneath the deformation front in the Tumaco segment, the oceanic basement is 2 to 2.1 km deeper than beneath the Patia and Manglares segments (Figure 12a). This deepening correlates with an increase in slab dip calcu-

lated from the wide-angle-derived velocity structure. Within 50 km landward of the deformation front, the mean slab dip on line SIS-47 is 11° compared to 6.5° for line SIS-40 and 7.5° for line SIS-42 (Figure 12b). Along the Tumaco segment, on every MCS lines there are eastward dipping normal faults in the crust of the Nazca Plate around the deformation front and beneath the lower continental slope (Figure 3b). These faults result in a deepening of the incoming plate and a local increase in slab dip. At the deformation front, this deepening also correlates with trench fill thickening, which is more than twice as thick on line SIS-47 as that on line SIS-40 and 40% thicker than on line SIS-42 (Figure 12c). To demonstrate the variations of heat flow without the influence of plate age, we arbitrarily set the Nazca Plate age at 15 Ma (Figure 12c) and kept all other parameters constant. These calculations show that the modeled heat flow is lower (60 mW m⁻²) on line SIS-47 in the Tumaco segment, than on lines SIS-40 (90 mW m⁻²)

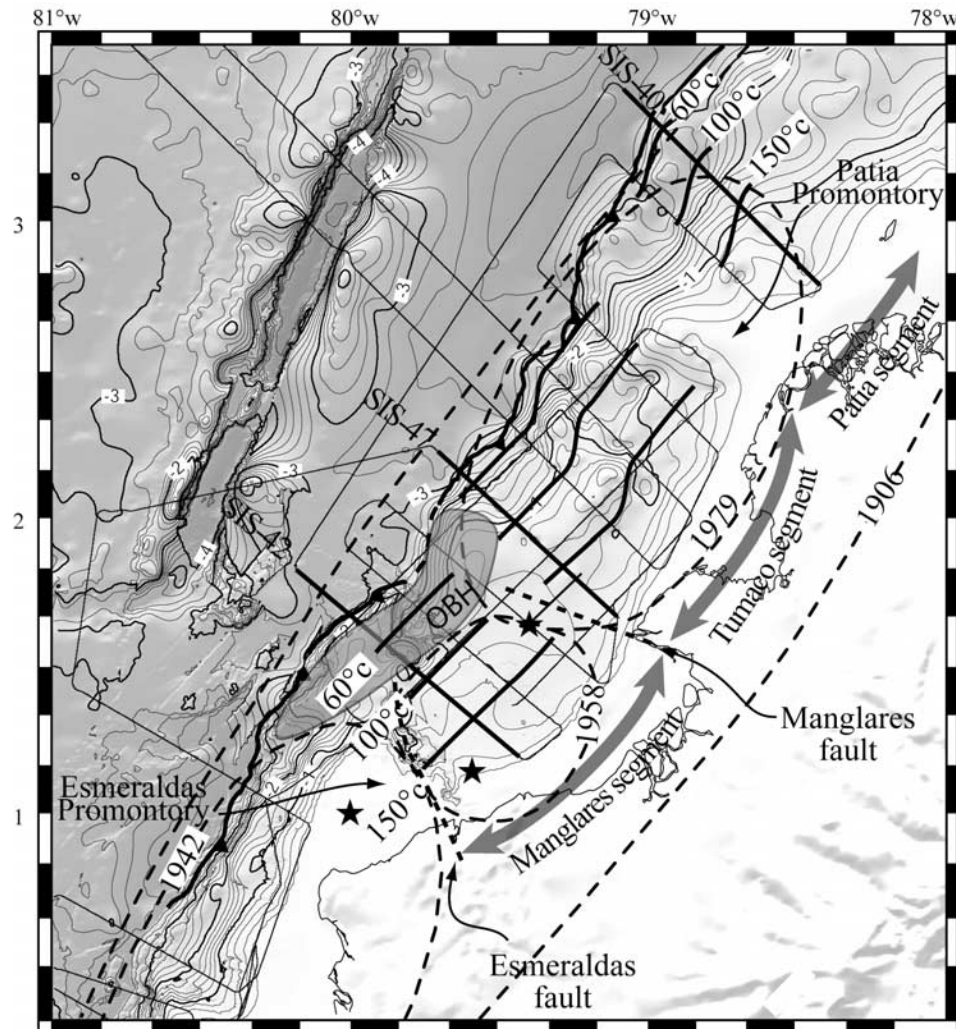


Figure 11. Location of the 60°, 100°, and 150°C isotherms across the NESC margin. Thick black margin-normal lines are SIS-40, SIS-47, and SIS-42 profiles used for thermal modeling. Note that these isotherms are laterally offset by at least $\sim 5 \pm 3$ km across the Manglares fault. Dashed ellipses and stars are rupture zones and epicenters of the great subduction earthquakes.

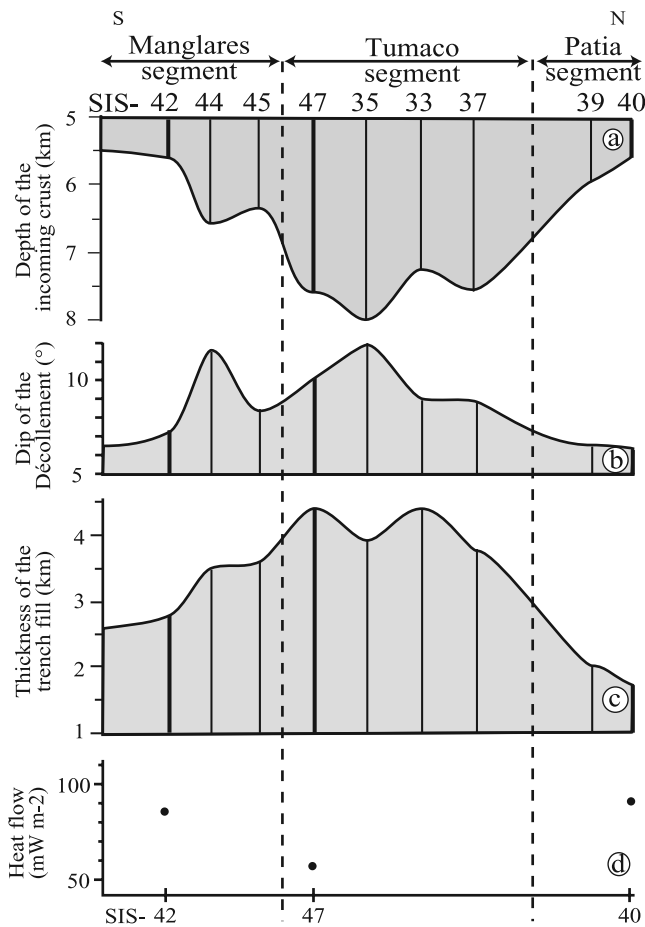


Figure 12. Along-strike variation of the (a) depth below seafloor to the top of the downgoing crust, picked from MCS dip lines at the deformation front, (b) dip of the décollement within 50 km from the deformation front, and (c) thickness of trench fill from seafloor to top of downgoing crust picked from MCS dip lines at the deformation front. To convert times to depths, we used velocities from wide-angle modeling. (d) Influence of these parameters on the calculated heat flow at the deformation front for lines SIS-40, SIS-47, and SIS-42, assuming an oceanic crustal age of 15 Myr and all other parameters constant for all lines.

and SIS-42 (87 mW m^{-2}) in the Manglares and Patia segments.

5.2.3. Influence of Hydrothermal Cooling

[32] The BSR-derived heat flow is 15 mW m^{-2} lower than the model-predicted heat flow within $\sim 10 \text{ km}$ of the deformation front for line SIS-47 (Figure 9). Circulation of fluids in the fractured upper crust of the subducting plate has been proposed by Langseth and Silver [1996] to account for the very low heat flow values of $\sim 28 \text{ mW m}^{-2}$ reported at the Costa Rica margin. Thermal models that incorporate the effect of hydrothermal cooling predict a landward increase in surface heat flow in agreement with observations [Harris and Wang, 2002]. Moreover, hydrothermal cooling is expected to result in low average heat flows seaward of the trench as observed by Langseth and Silver [1996] off Costa Rica. Nevertheless, near the location of

these low heat flows, some high heat flow values suggest large and abrupt variations along the Costa Rica margin [Fisher *et al.*, 2003]. We speculate that similar hydrothermal cooling is an additional process that may be locally responsible for the low heat flow values near the deformation front along line SIS-47 in the Tumaco segment.

5.3. Temperature and Depths of Megathrust Earthquakes

[33] The projection parallel to the trench of the 1958 hypocenter [Mendoza and Dewey, 1984] onto line SIS-42 (Figure 13c) suggests that the earthquake nucleated $\sim 70 \text{ km}$ landward of the deformation front, near the 170°C isotherm (Figure 11). Collot *et al.* [2004] proposed that the 1979 event initiated beneath the Manglares fault or immediately north of it and ruptured the entire Tumaco and Patia segments. Similarly, the projection of the 1979 hypocenter onto line SIS-47 (Figure 13b), although closer to the deformation front ($\sim 60 \text{ km}$) than the 1958 event, indicates a nucleation also near the 170°C isotherm (Figure 11). We note that location errors of the epicenters may reach 20 km [Mendoza and Dewey, 1984] and the intersections of isotherms with the megathrust have errors of at least $\pm 4 \text{ km}$ horizontally. However, for both 1958 and 1979 events, the location of the earthquake nucleation and the 170°C isotherm appear to be correlated, within the estimated errors.

5.4. Updip Limit of the NESC Margin Seismogenic Zone

[34] The seismogenic zone can be approximated by the area of coseismic failure [Swenson and Beck, 1996] and distribution of the aftershocks with thrust focal mechanisms as assumed by Mendoza and Dewey [1984] for the Ecuador–Colombia margin and by Pacheco *et al.* [1993] for other subduction zones. The fault plane solutions of the 1942, 1958 and 1979 aftershocks have never been published. Nevertheless, Mendoza and Dewey [1984] and Swenson and Beck [1996] interpreted these aftershocks as “events involved in strain release along a single fault system” and “events consistent with shocks occurring along the same interplate contact” indicating that these aftershocks are interpreted as thrust faulting events.

[35] For the 1942 and 1979 earthquakes, the coseismic rupture defined by inversion of seismic data as well as the zone of aftershocks that occurred within 3 months after the main shocks, extended as far seaward as the trench [Beck and Ruff, 1984; Mendoza and Dewey, 1984; Swenson and Beck, 1996]. We note, however, that observations from many subduction zones and the theory of the mechanics of submarine wedges [Wang and Hu, 2006] suggest that the megathrust seismogenic zone usually does not extend to the deformation front.

[36] In contrast, the updip limit of the aftershock zone and the rupture zone of the 1958 event are clearly located landward of the trench [Mendoza and Dewey, 1984]. We thus infer that there is a clear landward offset of the updip limit of the seismogenic zone of the 1958 earthquake relative to the 1942 and 1979 events as shown by the consistent offset of both the rupture zone and the aftershock distribution. Thus our thermal models suggest that the temperature at the updip limit of the seismogenic zone of

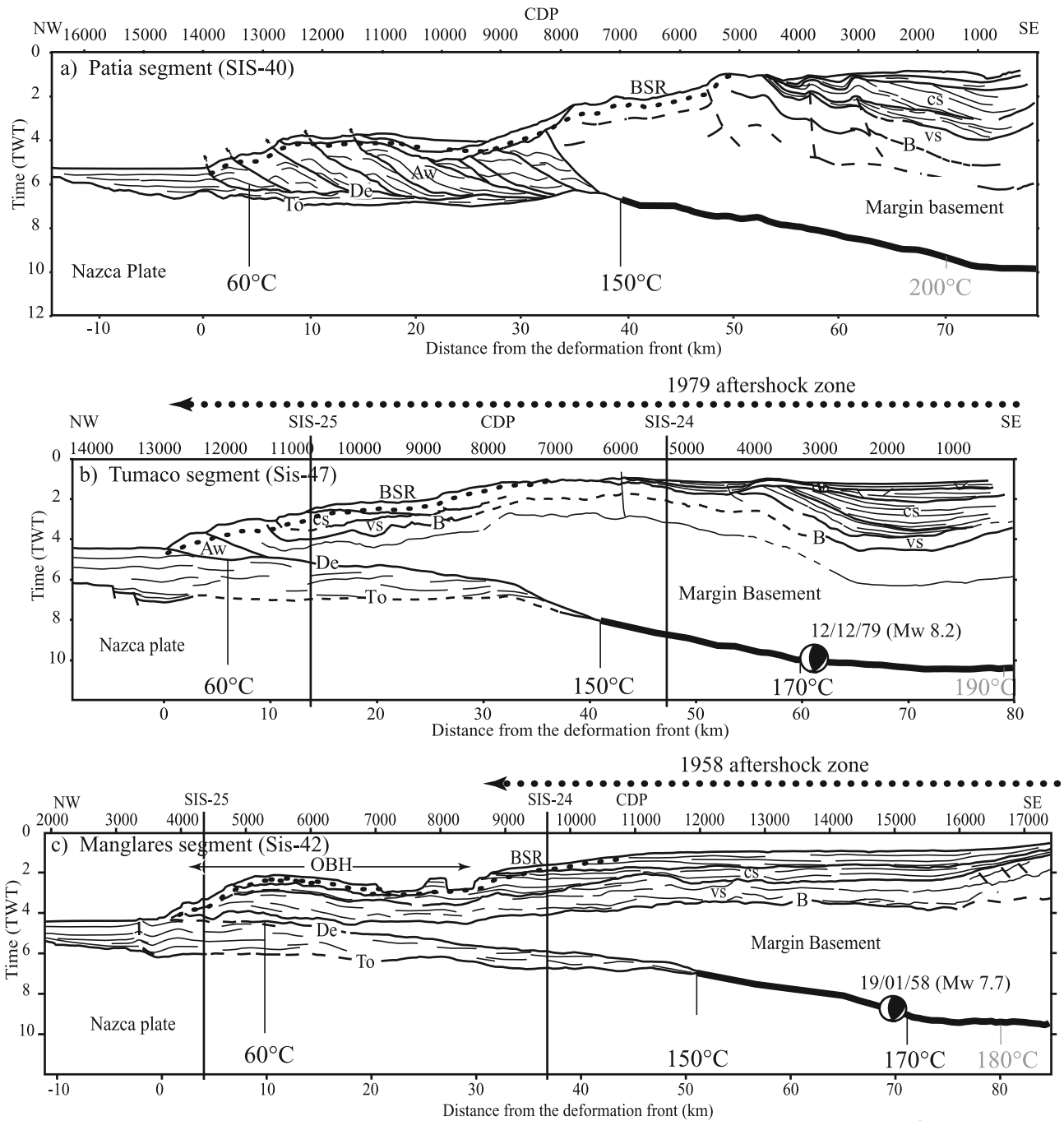


Figure 13. Location of the intersections between specific isotherms and the interpreted interplate thrust fault for the (a) Patia (SIS-40), (b) Tumaco (SIS-47), and (c) Manglares (SIS-42) margin segments. The shaded deepest isotherms are imprecisely located. The 1958 and 1979 earthquake focal mechanisms are projected onto the seismic sections parallel to the trench in the Tumaco reentrant. The seismogenic zone defined using the 150°C temperature as the updip limit is marked by the thick interface segment; however, the seismogenic zone likely extends farther toward the trench, as indicated by the seaward extent of the aftershocks zone. To, De, B, Aw, cs, and vs are as in Figure 3. Note that the 1958 and 1979 subduction earthquakes may have initiated at a temperature ~170°C.

the 1979 earthquake is clearly <100°C, possibly ~60°C, while it is ~100°C or more for the 1958 event.

[37] The 100 and 150°C isotherms are frequently correlated to the updip limit of the seismogenic zone [Hyndman et al., 1997; Oleskevich et al., 1999]. This correlation is

consistent with estimated temperature of transformation from smectite (exhibiting stable sliding behavior) to illite (exhibiting stick-slip behavior) [Vrolijk, 1990]. However, recent laboratory experiments, designed to investigate the frictional behavior of natural and synthetic clay-rich gouges,

suggest that a wide range of mechanical and chemical processes that are active at temperatures of $\sim 60^\circ$ to $\sim 150^\circ\text{C}$ may be more important than clay transformation in controlling the onset of stick slip on the thrust fault [Saffer and Marone, 2003]. On the NESC margin, the correlation between the updip limit of the seismogenic zone and 50 to 60°C isotherms support the hypothesis that the transition from stick slip to sliding behavior is controlled by very low temperature processes on the thrust fault.

[38] In a previous study of the MCS lines located in the region of the 1958 rupture zone, it was emphasized that in the frontal part of this margin segment there is a prominent outer basement high (OBH) and a major splay fault [Collot *et al.*, 2004]. The spatial correlation between the OBH, the splay fault, and the updip limit of the rupture zone suggests that the OBH may have behaved as a deformable buttress remaining coupled to the downgoing plate during the coseismic period, causing seaward rupture propagation along the splay fault [Collot *et al.*, 2004]. In this model, the thrust motion along the splay fault is followed by aseismic slip along the décollement beneath the OBH after the earthquake. The aftershock area also appears to be limited landward of the OBH, suggesting that the seismogenic zone of the 1958 event did not reach the trench. We propose that on the NESC margin the seismogenic zone in general reaches a position near the trench where it is possibly limited by very low temperature ($\sim 60^\circ\text{C}$) processes, except in the 1958 event area where its updip limit is more likely related to prominent structural features.

6. Conclusions

[39] Heat flow patterns on the north Ecuador–south Colombia margin have been determined using variations in the depth of the BSR identified on multichannel seismic reflection data. To investigate the thermal control on the seismogenic zone and megathrust earthquakes in this region, we have developed two-dimensional steady state thermal models for the NESC subduction zone. The conclusions of this study can be summarized as follows:

[40] 1. At the deformation front, coherent heat flow values are determined from several MCS lines for each morphotectonic segment of the margin: 100–110 mW m^{-2} for the Patia segment, 55–60 mW m^{-2} for the Tumaco segment, and 70–80 mW m^{-2} for the Manglares segment. For all segments, heat flow decreases to values of 40–50 mW m^{-2} at a distance of 25 km landward of the trench. The landward decreasing values, consistent with previous studies of heat flow at convergent margins, are related to the downward movement of subducting lithosphere and the landward thickening of the upper plate.

[41] 2. We have developed thermal models along three cross sections, which represent respectively the Patia, Tumaco and Manglares segments. The differences in thermal structure between these three margin segments result primarily from the age and dip variations of the 12–20 Myr incoming Nazca Plate. The heat flow variations at the deformation front also reflect the effects of the presence or absence of an accretionary prism or its volume, the subduction channel thickness, and the seaward extent and thickness of the fore-arc basin. Locally, hydrothermal cool-

ing may be responsible for remarkably low heat flow values within 10 km of the deformation front.

[42] 3. Our thermal models suggest that the 1958 and 1979 earthquakes nucleated within a central to shallow portion of the seismogenic zone, at temperatures estimated to be $\sim 170^\circ\text{C}$.

[43] 4. On the NESC margin, the aftershock zone and the rupture zone of the 1942 and 1979 earthquakes may have reached a position near the trench where the temperature is as low as $50^\circ\text{--}60^\circ\text{C}$. In contrast, the aftershock zone of the 1958 event is clearly restricted to a region landward of the outer basement high and a splay fault where the temperature on the thrust fault appears to be at least $\sim 100^\circ\text{C}$. These thermal models thus suggest that on the NESC margin the updip limit of the seismogenic zone is generally controlled by low temperature ($50^\circ\text{--}60^\circ\text{C}$) processes, except for the 1958 event, where the updip limit of the seismogenic zone is more likely related to prominent structural features in the upper plate landward of the deformation front.

References

- Abe, K. (1979), Size of great earthquakes of 1837–1974 inferred from tsunami data, *J. Geophys. Res.*, *84*, 1561–1568.
- Agudelo, W. (2005), Imagerie sismique quantitative de la marge convergente d'Equateur-Colombie, Ph.D. thesis, Univ. de Pierre et Marie Curie, Paris.
- Agudelo, W., P. Charvis, J.-Y. Collot, B. Marcaillou, and F. Michaud (2002), Structure of the southwestern Colombia convergent margin from the Sisteur seismic reflection-refraction experiment, paper presented at EGS XXVII, Eur. Geophys. Soc., Nice, France.
- Agudelo, W., A. Ribodetti, J.-Y. Collot, S. Operto, and B. Delouis (2005), Small scale seismic velocities and change in fluid pressure along the décollement by 2D quantitative imaging, *Eos Trans. AGU*, *86*(52), *Fall Meet. Suppl.*, Abstract T53B-1418.
- Beardmore, G. R., and J. P. Cull (2001), *Crustal Heat Flow: A Guide to Measurement and Modelling*, 324 pp., Cambridge Univ. Press, New York.
- Beck, S. L., and L. J. Ruff (1984), The rupture process of the great 1979 Colombia earthquake: Evidence for the asperity model, *J. Geophys. Res.*, *89*, 9281–9291.
- Bourgeois, J., C. Petroff, H. Yeh, V. Titov, C. E. Synolakis, B. Benson, J. Kuroiwa, J. Lander, and E. Norabuena (1999), Geologic setting, field survey and modelling of the Chimbote, northern Peru, tsunami of 21 February 1996, *Pure Appl. Geophys.*, *154*, 513–540.
- Brown, G. C., and A. E. Mussett (1993), *The Inaccessible Earth: An Integrated View to Its Structure and Composition*, CRC Press, Boca Raton, Fla.
- Cermak, V., L. Bodri, L. Rybach, and G. Buntebarch (1990), Relationship between seismic velocity and heat production: Comparison of two sets of data and test of validity, *Earth Planet. Sci. Lett.*, *99*, 48–57.
- Chael, E. P., and G. S. Stewart (1982), Recent large earthquakes along the middle America trench and their implications for the subduction process, *J. Geophys. Res.*, *87*, 329–338.
- Clauser, C., and E. Huenges (1995), Thermal conductivity of rocks and minerals, in *Rock Physics and Phase Relations: A handbook of Physical Constants*, edited by T. J. Ahrens, pp. 105–126, AGU, Washington, D. C.
- Collot, J.-Y., P. Charvis, M. A. Gutscher, and S. Operto (2002), Exploring the Ecuador–Colombia active margin and interplate seismogenic zone, *Eos Trans. AGU*, *83*(17), 189–190.
- Collot, J.-Y., B. Marcaillou, F. Sage, F. Michaud, W. Agudelo, P. Charvis, D. Grandorge, M. A. Gutscher, and G. D. Spence (2004), Are rupture zone limits of great subduction earthquakes controlled by upper plate structures? Evidence from multichannel seismic reflection data acquired across the northern Ecuador–southwest Colombia margin, *J. Geophys. Res.*, *109*, B11103, doi:10.1029/2004JB003060.
- Cosma, L., H. Lapiere, E. Jaillard, G. Laubacher, D. Bosch, A. Desmet, M. Mamberti, and P. Gabrielle (1998), Pétrographie et Géochimie des unités magmatiques de la Cordillère occidentale d'Equateur ($0^\circ 30'$): Implications tectoniques, *Bull. Soc. Geol. Fr.*, *169*(6), 739–751.
- Currie, C. A., R. D. Hyndman, K. Wang, and V. Kostoglodov (2002), Thermal models of the Mexico subduction zone: Implications for the megathrust seismogenic zone, *J. Geophys. Res.*, *107*(B12), 2370, doi:10.1029/2001JB000886.

- Deniaud, Y. (2000), Enregistrement sédimentaire et structural de l'évolution géodynamique des Andes Equatoriennes au cours du Néogène: Étude des bassins d'avant-arc et bilan de masse, Ph.D. thesis, Univ. Joseph Fourier, Grenoble, France.
- Dickens, G. R., and M. S. Quinby-Hunt (1994), Methane hydrate stability in seawater, *Geophys. Res. Lett.*, *21*, 2115–2118.
- Dumitru, T. A. (1991), Effects of subduction parameters on geothermal gradients in forearcs, with an application to Franciscan subduction in California, *J. Geophys. Res.*, *96*, 621–641.
- Engdahl, E. R., R. P. Van der Hilst, and R. P. Buland (1998), Global teleseismic earthquake relocation with improved travel times and procedures for depth determination, *Bull. Seismol. Soc. Am.*, *88*, 722–743.
- Evans, C. D. R., and J. E. Whittaker (1982), The geology of the western part of the Borbón Basin, northwest Ecuador, in *Trench-Forearc Geology*, edited by J. K. Leggett, *Geol. Soc. London Spec. Publ.*, *10*, 191–198.
- Fisher, A. T., C. A. Stein, R. N. Harris, K. Wang, E. A. Silver, M. Pfender, M. Hutnak, A. Cherkaoui, R. Bodzin, and H. Vilinger (2003), Abrupt thermal transition reveals hydrothermal boundary and role of seamounts within the Cocos Plate, *Geophys. Res. Lett.*, *30*(11), 1550, doi:10.1029/2002GL016766.
- Flueh, E. R., J. Bialas, and P. Charvis (2001), Cruise report SO159–Salieri, 256 pp., Leibniz-Inst. für Meereswiss. an der Univ. Kiel, Kiel, Germany.
- Gailler, A., P. Charvis, V. Sallares, J.-Y. Collot, D. Graindorge, and A. Calahorrano (2003), Structure of the subduction channel at the Ecuador-Carnegie Ridge convergent margin from seismic modelling and inversion, *Geophys. Res. Abstr.*, *5*, Abstract 10867.
- Gailler, A., P. Charvis, S. Operto, J.-Y. Collot, and E. R. Flueh (2004), Modelling of the subduction channel along the Ecuadorian convergent margin using wide-angle seismic data, *Geophys. Res. Abstr.*, *6*, Abstract 05745.
- Ganguly, N., G. D. Spence, N. R. Chapman, and R. D. Hyndman (2000), Heat flow variations from bottom simulating reflectors on the Cascadia margin, *Mar. Geol.*, *164*, 53–68.
- Gansser, A. (1973), Facts and theories on the Andes, *J. Geol. Soc. London*, *129*, 93–131.
- Goossens, P. J., and W. I. Rose (1973), Chemical composition and age determination of tholeiitic rocks in the basic igneous complex, Ecuador, *Geol. Soc. Am. Bull.*, *84*, 1043–1052.
- Hamilton, E. L. (1980), Geoacoustic modelling of the seafloor, *J. Acoust. Soc. Am.*, *68*(5), 1313–1340.
- Hardy, N. C. (1991), Tectonic evolution of the easternmost Panama Basin: Some new data and interferences, *J. S. Am. Earth Sci.*, *4*(3), 261–269.
- Harris, R. N., and K. Wang (2002), Thermal models of the Middle America Trench at the Nicoya Peninsula, Costa Rica, *Geophys. Res. Lett.*, *29*(21), 2010, doi:10.1029/2002GL015406.
- Heasler, H. P., and R. C. Surdam (1985), Thermal evolution of coastal California with application to hydrocarbon maturation, *AAPG Bull.*, *69*, 1386–1400.
- Henry, S. A., S. Ellis, and C. I. Uruski (2003), Conductive heat flow variations from bottom-simulating reflectors on the Hikurangi margin, New Zealand, *Geophys. Res. Lett.*, *30*(2), 1065, doi:10.1029/2002GL015772.
- Herd, D. G., T. L. Youd, H. Meyer, J. L. C. Arango, W. J. Person, and C. Mendoza (1981), The Great Tumaco, Colombia earthquake of 12 December 1979, *Science*, *211*, 441–445.
- Hyndman, R. D., and K. Wang (1993), Thermal constraints on the zone of the major thrust earthquakes failure: The Cascadia subduction zone, *J. Geophys. Res.*, *98*, 2039–2060.
- Hyndman, R. D., and K. Wang (1995), The rupture zone of the Cascadia great earthquakes from current deformation and the thermal regime, *J. Geophys. Res.*, *100*(B11), 22,133–22,154.
- Hyndman, R. D., K. Wang, and M. Yamano (1995), Thermal constraints on the seismogenic portion of the southwestern Japan subduction thrust, *J. Geophys. Res.*, *100*(B8), 15,373–15,392.
- Hyndman, R. D., M. Yamano, and D. A. Oleskevich (1997), The seismogenic zone of subduction thrust faults, *Isl. Arcs*, *6*(3), 244–260.
- Jaillard, E., M. Ordoñez, S. Benítez, G. Berrones, N. Jimenez, G. Montenegro, and I. Zambrano (1995), Basin development in an accretionary, oceanic-floored fore-arc setting: Southern coastal Ecuador during late Cretaceous–late Eocene time, in *Petroleum Basins of South America*, edited by A. J. Tankard, R. Suarez, and H. J. Welsink, pp. 615–631, Am. Assoc. of Pet. Geol., Tulsa, Okla.
- Juteau, T., F. Mégard, L. Raharison, and H. Whitechurch (1977), Les assemblages ophiolitiques de l'océan équatorial: Nature pétrographique et position structurale, *Bull. Soc. Geol. Fr.*, *19*, 1127–1132.
- Kanamori, H. (1986), Rupture process of subduction zone earthquakes, *Annu. Rev. Earth Planet. Sci.*, *14*, 293–322.
- Kanamori, H., and J. W. Given (1981), Use of long-period surface waves for rapid determination of earthquake-source parameters, *Phys. Earth Planet. Inter.*, *27*, 8–31.
- Kanamori, H., and K. C. McNally (1982), Variable rupture mode of the subduction zone along the Ecuador–Colombia coast, *Bull. Seismol. Soc. Am.*, *72*(4), 1241–1253.
- Kato, N., and T. Seno (2003), Hypocenter depths of large interplate earthquakes and their relation to seismic coupling, *Earth Planet. Sci. Lett.*, *210*, 53–63.
- Kelleher, J. (1972), Rupture zones of large South American earthquakes and some predictions, *J. Geophys. Res.*, *77*, 2087–2103.
- Langseth, M. G., and E. A. Silver (1996), The Nicoya convergent margin: A region of exceptionally low heat flow, *Geophys. Res. Lett.*, *23*(8), 891–894.
- Lockridge, P. A., and R. H. Smith (1984), Tsunamis in the Pacific Basin 1900–1983, map, Natl. Environ. Satell., Data, and Inf. Serv., Boulder, Colo.
- Marcaillou, B. (2003), Régimes tectoniques et thermiques de la marge nord Équateur–sud Colombie (0°–3,5°N)—Implications sur la sismogénèse., Ph.D. thesis, Univ. de Pierre et Marie Curie, Paris.
- Marcaillou, B., G. D. Spence, J.-Y. Collot, K. Wang, and A. Ribodetti (2005), Thermal regime from bottom simulating reflectors along the N Ecuador–S Colombia margin: Relation between tectonic segmentation, thermal variation and the limit of the seismic rupture zones, *Eos Trans. AGU*, *86*(52), Fall Meet. Suppl., Abstract T41F-04.
- Marone, C., and C. H. Scholz (1988), The depth of seismic faulting and the upper transition from stable to unstable slip regimes, *Geophys. Res. Lett.*, *15*, 621–624.
- Meissner, R. O., E. R. Flueh, F. Stibane, and E. Berg (1976), Dynamics of the active plate boundary in southwest Colombia according to recent geophysical measurements, *Tectonophysics*, *35*, 115–136.
- Mendoza, C., and J. W. Dewey (1984), Seismicity associated with the great Colombia–Ecuador earthquakes of 1942, 1958 and 1979: Implications for barrier models of earthquake rupture, *Bull. Seismol. Soc. Am.*, *74*(2), 577–593.
- Moore, J. C., and D. M. Saffer (2001), Updip limit of the seismogenic zone beneath the accretionary prism of southwest Japan: An effect of diagenetic to low-grade metamorphic processes and increasing effective stress, *Geology*, *29*(2), 183–186.
- Mountney, N. P., and G. K. Westbrook (1997), Quantitative analysis of Miocene to recent forearc basin evolution along the Colombian margin, *Basin Res.*, *9*, 177–196.
- Nagai, R., M. Kikuchi, and Y. Yamanaka (2001), Comparative study on the source process of recurrent large earthquakes in Sanriku–Oki region: The 1968 Tokachi–Oki and the 1994 Sanriku–Oki earthquake., *J. Seismol. Soc. Jpn.*, *52*, 267–289.
- Oleskevich, D. A., R. D. Hyndman, and K. Wang (1999), The updip and downdip limits to great subduction earthquakes: Thermal and structural models of Cascadia, south Alaska, SW Japan and Chile, *J. Geophys. Res.*, *104*, 14,965–14,991.
- Pacheco, J. F., L. R. Sykes, and C. H. Scholz (1993), Nature of seismic coupling along simple plate boundaries of the subduction type, *J. Geophys. Res.*, *98*, 14,133–14,159.
- Peacock, S. M., and R. D. Hyndman (1999), Hydrated mineral in the mantle wedge and the maximum depth of subduction thrust earthquakes, *Geophys. Res. Lett.*, *26*, 2517–2520.
- Pelayo, A. M., and D. A. Wiens (1990), The November 20, 1960 Peru tsunami earthquake: Source mechanism of a slow event, *Geophys. Res. Lett.*, *17*, 661–664.
- Peterson, E. T., and T. Seno (1984), Factors affecting seismic moment release rates in subduction zones, *J. Geophys. Res.*, *89*, 10,233–10,248.
- Ruppel, C. (1997), Anomalously cold temperatures observed at the base of gas hydrate stability zone on the US Atlantic passive margin, *Geology*, *25*, 699–702.
- Saffer, D. M., and C. Marone (2003), Comparison of smectite- and illite-rich gouge frictional properties: Application to the updip limit of the seismogenic zone along subduction megathrusts, *Earth Planet. Sci. Lett.*, *215*, 219–235.
- Sato, T., K. Imanishi, and M. Kosuga (1996), Three-stage rupture process of the 28 December 1994 Sanriku–Oki earthquake, *Geophys. Res. Lett.*, *23*, 33–36.
- Shipley, T. H., M. H. Houston, R. T. Buffer, F. J. Shaub, K. J. McMillen, J. W. Ladd, and J. L. Worzel (1979), Seismic evidence for widespread possible gas hydrate horizons on continental slopes and rises, *AAPG Bull.*, *63*, 2204–2213.
- Sibson, R. H. (1982), Fault zone models, heat flow and the depth distribution of earthquakes in the continental crust of the United States, *Bull. Seismol. Soc. Am.*, *72*, 151–163.
- Spence, W., C. Mendoza, E. R. Engdahl, G. L. Choy, and E. Norabuena (1999), Seismic subduction of the Nazca Ridge as shown by the 1996–97 Peru earthquakes, *Pure Appl. Geophys.*, *154*, 753–776.

- Stein, C. A., and S. Stein (1992), A model for the global variation in oceanic depth and heat flow with lithospheric age, *Nature*, *359*, 123–129.
- Suess, E., and R. von Huene (1988), *Proceedings of the Ocean Drilling Program Initial Report, Leg 112*, 1015 pp., Ocean Drill. Program, College Station, Tex.
- Swenson, J. L., and S. L. Beck (1996), Historical 1942 Ecuador and 1942 Peru subduction earthquakes, and earthquake cycles along Colombia–Ecuador and Peru subduction segments, *Pure Appl. Geophys.*, *146*, 67–101.
- Tavera, H., E. Buforn, I. Bernal, Y. Antayhua, and L. Vilacapoma (2002), The Arequipa (Peru) earthquake of June 23, 2001, *J. Seismol.*, *6*, 279–283.
- Thatcher, W. (1990), Order and diversity in the modes of circum-Pacific earthquake recurrence, *J. Geophys. Res.*, *95*, 2609–2623.
- Toussaint, J.-F., and J. J. Restrepo (1994), The Colombian Andes during Cretaceous times, in *Cretaceous Tectonics of the Andes*, edited by J. A. Salfity, pp. 61–100, Vieweg, Braunschweig, Germany.
- Townend, J. (1997), Estimates of conductive heat flow through bottom-simulating reflectors on the Hikurangi and southwest Fiordland continental margins, *N. Z. Mar. Geol.*, *141*, 209–220.
- Trenkamp, R., J. N. Kellogg, J. T. Freymueller, and H. P. Mora (2002), Wide plate margin deformation southern Central America and northwestern South America, CASA GPS observations, *J. S. Am. Earth Sci.*, *15*, 157–171.
- Turcotte, D. L., D. C. McAdoo, and J. G. Caldwell (1978), An elastic-perfectly plastic analysis of the bending of the lithosphere at a trench, *Tectonophysics*, *47*, 193–205.
- Valdez, C., R. P. Meyer, R. Zuniga, J. Havskov, and S. K. Singh (1982), Analysis of the Petatlan aftershocks: Number, energy release and asperities, *J. Geophys. Res.*, *87*, 8519–8527.
- Van den Beukel, J., and R. Wortel (1988), Thermo-mechanical modelling of arc-trench regions, *Tectonophysics*, *154*, 177–193.
- Vrolijk, P. (1990), On the mechanical role of smectite in subduction zones, *Geology*, *18*, 703–707.
- Wang, K., and E. E. Davis (1992), Thermal effects of marine sedimentation in hydrothermally active areas, *Geophys. J. Int.*, *110*, 70–78.
- Wang, K., and Y. Hu (2006), Accretionary prisms in subduction earthquake cycles: The theory of dynamic Coulomb wedge, *J. Geophys. Res.*, *111*, B06410, doi:10.1029/2005JB004094.
- Wang, K., R. D. Hyndman, and D. Davis (1993), Thermal effects of sediment thickening and fluid expulsion in accretionary prisms: Model and parameter analysis, *J. Geophys. Res.*, *98*, 9975–9984.
- Wang, K., R. D. Hyndman, and M. Yamano (1995a), Thermal regime of the southwest Japan subduction zone: Effects of age history of the subducting plate, *Tectonophysics*, *248*, 53–69.
- Wang, K., T. Mulder, G. C. Rogers, and R. D. Hyndman (1995b), Case for very low coupling stress on the Cascadia subduction fault, *J. Geophys. Res.*, *100*, 12,907–12,918.
- Xu, W., and C. Ruppel (1999), Predicting the occurrence, distribution, and evolution of methane gas hydrate in porous sediments, *J. Geophys. Res.*, *104*, 5081–5095.
- Yamano, M., S. Uyeda, A. Y. Aoki, and T. H. Shipley (1982), Estimates of heat flow derived from gas hydrates, *Geology*, *10*, 339–343.

J.-Y. Collot, Geosciences Azur, Institut de la Recherche pour le Développement, B.P. 48, Quai de la Darse, F-06235 Villefranche sur mer, France. (marcaill@obs-vlfr.fr)

B. Marcaillou and G. Spence, School of Earth and Ocean Science, University of Victoria, Victoria, BC, Canada V8W 2Y2.

K. Wang, Pacific Geoscience Center, 9860 West Saanich Road, Sydney, BC, Canada V8L 4B2.